JACS
JOURNAL OF THE AMERICAN CHEMICAL SOCIETY
Article
pubs.acs.org/JACS

Contact Line Motion on Nanorough Surfaces: A Thermally Activated Process

Melanie Ramiasa, John Ralston,* Renate Fetzer,† Rossen Sedev, Doris M. Fopp-Spori,‡ Christoph Morhard,§ Claudia Pacholski,§ and Joachim P. Spatz§

Ian Wark Research Institute, University of South Australia, Mawson Lakes, South Australia 5095, Australia

Supporting Information

ABSTRACT: The motion of a solid−liquid−liquid contact line over nanorough surfaces is investigated. The surface nanodefects are varied in size, density, and shape. The dynamics of the three-phase contact line on all nanorough substrates studied is thermally activated. However, unlike the motion of a liquid−vapor interface over smooth surfaces, this thermally activated process is not adequately described by the molecular kinetic theory. The molecular parameters extracted from the experiments suggest that on the nanorough surfaces, the motion of the contact line is unlikely to simply consist of molecular adsorption−desorption steps. Thermally activated pinning−depinning events on the surface nanodefects are also important. We investigate the effect of surface nanotopography on the relative importance of these two mechanisms in governing contact line motion. Using a derivation for the hysteresis energy based on Joanny and de Gennes's model, we evaluate the effect of nanotopographical features on the wetting activation free energy and contact line friction. Our results suggest that both solid−liquid interactions and surface pinning strength contribute to the energy barriers hindering the three-phase contact line motion. For relatively low nanodefect densities, the activation free energy of wetting can be expressed as a sum of surface wettability and surface topography contributions, thus providing a direct link between contact line dynamics and roughness parameters.

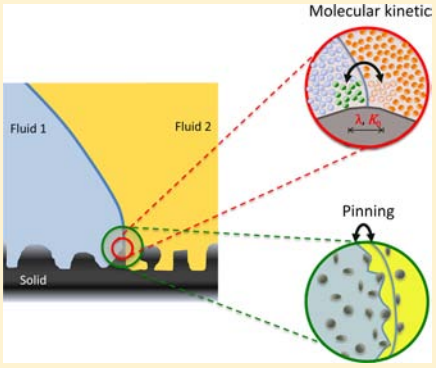

INTRODUCTION AND THEORETICAL BACKGROUND

The wetting of structured surfaces is of great interest in many fields of applied science, such as microfluidics, coating, printing, microelectronics, and self-cleaning materials. It is well-known that surface microroughness influences both static wettability and static contact angle hysteresis. However, our knowledge of the impact of nanodefects on static and dynamic wetting is still very limited.

In previous work we have shown that the dynamics of the three-phase contact line (TPCL) on a substrate decorated with 15 nm spherical particles is thermally activated.[1,2] However, unlike the motion of a liquid−vapor interface over smooth surfaces, this thermally activated process was not completely described by the molecular kinetic theory (MKT) of Blake and Haynes.[3] Although the experimental dynamic contact angle data could be fitted well by the Blake model, the molecular parameters extracted from these fits were not consistent with molecular adsorption−desorption processes. We argued that thermally activated pinning−depinning on the surface nanodefects could be the reason for this discrepancy. However, at the very small roughness scale examined (<20 nm), no definite conclusion could be drawn as to the relative importance of one or the other mechanisms in the overall contact line motion. In the work presented here, we deepen our analysis of the relative contribution of molecular adsorption and pinning events when a water−dodecane interface moves across various nanorough substrates. The size of the spherical nanodefects was between 50 and 75 nm, for a broad range of surface densities. Two additional surfaces featuring nanodefects with sharp edges (pillars and cones) at a fixed surface density were also investigated.

Dynamic wetting and dewetting have been investigated for a wide range of systems.[4,5] When the motion of the TPCL is slow (typically below 0.01 m/s) and viscous dissipation can be neglected, contact line dynamics is generally well-described by the MKT:[3,4]

$$U = 2K_0\lambda\sinh\left[\frac{\gamma(\cos\theta_0 - \cos\theta_D)\lambda^2}{2k_BT}\right] \quad (1)$$

where U is the TPCL velocity, γ is the surface tension between the two fluids, θ_0 is the static contact angle, and θ_D the macroscopic dynamic contact angle. The molecular parameters K_0 and λ characterize the thermally activated displacements occurring in the vicinity of the contact line: λ is the average displacement length, while K_0 is the equilibrium frequency. The latter can be written in terms of wetting activation free energy, ΔG_w^*:

Received: October 24, 2012
Published: April 22, 2013

   dx.doi.org/10.1021/ja3104846 | J. Am. Chem. Soc. 2013, 135, 7159−7171

$$K_0 = \frac{k_B T}{h} \exp\left(-\frac{\Delta G_w^*}{N_A k_B T}\right) \quad (2)$$

When the argument of the sinh is much smaller than unity, which is the case when $\theta_D \sim \theta_0$, eq 1 becomes[6]

$$U = \frac{\gamma(\cos\theta_0 - \cos\theta_D)K_0\lambda^3}{k_B T} = \frac{1}{\zeta}F_w \quad (3)$$

where $F_w = \gamma\ (\cos\theta_0 - \cos\theta_D)$ is the out of balance surface tension force driving the contact line motion, and the contact line friction coefficient $\zeta = k_B T/K_0\lambda^3$ quantifies the energy dissipation in the three-phase zone. In the original model,[3] the contact line motion is believed to be solely governed by the interactions between the solid surface and the fluids. Thus, initially, the local fluctuations of the contact line were expected to correspond to thermally activated adsorption−desorption processes occurring at the molecular scale, with λ in the angstrom range. When the original model was later amended to account for the influence of the fluid viscosity, the activation free energy of wetting was redefined as the sum of surface and viscous contributions, ΔG_s^* and ΔG_v^*:[7]

$$\Delta G_w^* = \Delta G_s^* + \Delta G_v^* \quad (4)$$

If it is assumed that the surface component of the specific activation free energy of wetting, $\Delta g_s^* = \Delta G_s^*/\lambda^2 N_A$, can be equated to the reversible work of adhesion between the solid and the advancing fluid,[8] then

$$\Delta g_s^* \sim W_a = \gamma(1 + \cos\theta_0) \quad (5)$$

We have shown[1,2] that the dependence of contact line friction on the solid−liquid interaction for the general case of two immiscible fluids moving across a solid surface is well described by

$$\zeta_{12} = \frac{(\eta_1 + \eta_2)v}{\lambda^3} \exp\left(\frac{\lambda^2\gamma_{12}(1 + \cos\theta_1)}{k_B T}\right) \quad (6)$$

where η_i is the viscosity of fluid i and γ_{12} is the fluid−fluid interfacial tension. This approach, based on a force balance analysis, accounts for the friction contribution in both fluids.

Although the experimental data from various dynamic wetting studies follow the general trend of eq 1, it is important to note that the exponential variation of the contact line velocity with the cosine of the dynamic contact angle only indicates that the dynamics is thermally activated. The real nature of the thermally activated steps controlling contact line motion remains uncertain. Indeed, while some studies involving simple fluids partially wetting smooth surfaces report displacement lengths λ in good agreement with the proposition of molecular adsorption−desorption processes (λ below 1 nm),[4,9−13] others found larger λ values, contradicting the single molecule jump hypothesis.[14−19] Rolley and Guthmann were the first to explain the large value of λ (∼10 nm), found in their innovative work with liquid helium wetting a substrate with nanoscopic defects.[16] They suggested that the mechanism governing contact line motion was a thermally activated pinning and depinning process.[17] In this approach, the pinning of the contact line controls both the static contact angle hysteresis and the dynamic wetting close to the depinning threshold (i.e., in the low velocity regime). The energy barrier impeding contact line motion depends on the strength of the contact line attachment to surface topographical defects. Their approach was supported by the good agreement found between the specific activation free energy, Δg_s^*, and the hysteresis energy[17]

$$H = \gamma(\cos\theta_r - \cos\theta_a) \quad (7)$$

where θ_r and θ_a are the static receding and advancing contact angles. These pioneering findings revealing the effect of nanoroughness on dynamic wetting were very important, given that it has been commonly accepted that roughness below 0.1 μm has no influence on static wettability and contact angle hysteresis.[20−24]

It is important to note that, alike in many others studies,[5,17] the hysteresis is here defined as an energy change per unit length of contact line and per unit length of displacement distance in J·m^{-2}. Some other groups have proposed to relate the parameters describing the contact angle hysteresis to the unit length of the triple line.[25−27] In this case the natural dimension of the energy hysteresis is J·m^{-1}. A rescaling of the hysteresis experimental data discussed in the present work can be performed by multiplying the data per the unit length of displacement. This procedure is independent of geometry, contact radius, or drop size and thus does not modify the numerical values. Following this approach, for consisteny purposes, one would then consider the specific activation energy per unit length, $\Delta G_w^*\ dR$, where dR is an incremental change in drop radius.

The model for contact angle hysteresis developed by Joanny and de Gennes (JG) was derived for heterogeneities in the micrometer range (typically much greater than 30 nm to 1 μm) and neglected thermal fluctuations.[28] In this theory, the effect of nanoscopic heterogeneities was originally neglected. However, surfaces which are smooth and homogeneous on the micrometer scale usually exhibit a degree of hysteresis, suggesting that hysteresis may be generated by nanometer heterogeneities. When the defect size is on the nanoscale (typically below 100 nm), the effect of thermal fluctuations and van der Waals forces on the interface shape can no longer be neglected.[29]

In recent years, driven by an increasing industrial interest in superhydrophobic and nanotextured surfaces, several static wetting studies have investigated the possible correlation between macroscopic hysteresis and nanoscopic properties of solid surfaces.[30−36] Ramos et al.[34] reported reasonable agreement between a simplified version of JG theory and their experimental results for nanorough surfaces. This correlation was very recently confirmed by the work of Delmas et al.[36] In an atomic force microscopy experiment designed to investigate contact angle hysteresis on nanodefects, they showed that the JG model[28] can successfully interpret the hysteresis energy at the level of the thermal energy dissipated on single nanodefects and that the minimum defect size necessary to produce contact angle hysteresis is of molecular dimensions.[36]

The JG model[28] for hysteresis is based on the energy necessary to depin a contact line anchored on a surface heterogeneity. Assuming that the contact line position is governed by a balance between the defect pinning strength deforming the meniscus, F_0, and the contact line elastic restoring force with a spring constant k, the energy dissipated in a jump as the contact line depins from a single defect (advancing or receding), W_d, is given by

dx.doi.org/10.1021/ja3104846 | J. Am. Chem. Soc. 2013, 135, 7159−7171

$$W_d = \frac{F_0^2}{2k} \tag{8}$$

For physical heterogeneities (i.e., roughness), the pinning force F_0 is[28,35,37]

$$F_0 = h\gamma[\cos(\theta_0 - \phi) - \cos\theta_0] \tag{9}$$

where h is the "size" of the defects, ϕ is the local defect slope, and θ_0 is the static contact angle on the corresponding smooth surface. The spring constant k, of the elastic force is given by

$$k = \frac{\pi\gamma\sin^2\theta_0}{\ln\frac{L}{h}} \tag{10}$$

where L is a large cutoff length which may be either the size of the droplet or the capillary length of the system. Accounting for the fact that, over a hysteresis cycle, a single defect should anchor the contact line in both advancing and receding directions of motion, and assuming that the same energy W_d is dissipated in both cases, the total energy dissipated around a hysteresis cycle, W, is:[28,34,35]

$$W = 2W_d = \frac{F_0^2}{k} \tag{11}$$

In practice the energy dissipated by a single defect in the advancing and receding direction is not the same and distinct W_d^{adv} and W_d^{rec} terms have to be evaluated separately.

If d is the defect density on the surface (number of defects per unit area) and h the defect size, assuming that the defect forces are simply additive for well-separated defects, i.e., $dh^2 \ll 1$ (Figure A1), Joanny and de Gennes[28] found that the hysteresis energy is

$$H_{JG} = dW \tag{12}$$

Around a single defect the contact line adopts a logarithmic shape, with long tails on both sides of the maximum deformation.[38] Thus one may argue that it is only possible to assume that the logarithmic deformations of the meniscus arising from individual defects do not interact, if the distance between two defects is larger than the cutoff length over which the contact line is deformed by a single defect $(1/hd) \gg L$. If the solid plane is vertical, the tail length is cut off by the capillary length, which describes the relative importance of hydrostatic and Laplace pressure. In this case the critical defect density above which the defects start to interact is $d_c \approx 1/L_c^2$, where $L_c = (\gamma/\Delta\rho g)^{1/2}$ is the capillary length,[39] and thus the defects' contribution to the contact line deformation is additive[28] only for dilute defects separated by more than L_c. Yet, when studying the spreading of small droplets, typically smaller in size than L_c, a smaller cutoff length is relevant. The critical defect density can be evaluated using the typical drop diameter.

The case of dense defect coverage is more complex because the defect contributions are not independent. The theoretical description of contact angle hysteresis is complicated by the cooperative effect of long-range capillary interactions, and no simple relationship between the overall hysteresis and the energy dissipated by a single defect has been reported as yet.[5]

In the JG approach, the respective effects of the defect size, shape, and density (via h, φ, and d, respectively) are explicitly accounted for in the hysteresis energy H_{JG}, thus providing a more detailed description of the influence of the real surface topography, compared with the hysteresis energy simply calculated from the macroscopic measurement of the advancing and receding contact angles (eq 7). Furthermore, the flow direction and possible asymmetry between advancing and receding contact line motion can be accounted for. The main disadvantage of the JG approach is that it is only valid for dilute defects.

Using the JG model to evaluate the hysteresis energy of nanorough surfaces may provide some insight into the importance of thermally activated pinning−depinning processes on contact line dynamics. Indeed, in their study of hysteresis at the nanoscale, Delmas et al.[36] found a pinning energy of the order of 10^{-20} J, rather close to the thermal energy $k_BT = 4.10^{-21}$ J. These results, similar to those of Rolley and Guthmann,[17] suggest that when the surface defects are nanoscopic, the effect of activated molecular dynamics and activated pinning on nanodefects becomes difficult to tell apart and both may play a role in influencing the overall contact line dynamics. Our study of dynamic wetting on surfaces with 15 nm spherical defects lent support to this hypothesis.[1] However, to the best of our knowledge, no dynamic wetting study has yet directly correlated the surface topographical parameters with the contact line velocity behavior.

In fact very few dynamic wetting studies have addressed the specific influence of surface nanoroughness. In their study of the spreading of squalane on heterogeneous Langmuir−Blodgett films,[40] Semal et al. were the first to investigate the effect of surface nanoroughness (RMS roughness below 1.5 nm) on the MKT parameters extracted from the experimental data. The values found for λ were in good agreement with the roughness scale. Furthermore, a linear increase in the activation free energy of wetting with surface nanoroughness was observed and was attributed to an increasing pinning potential of the rough surface. Semal et al.[40] proposed an amended version of eq 2 which includes the effect of surface roughness, r_{RMS}:

$$K_0 = \frac{k_BT}{h}\exp\left[-\frac{(\Delta G_w^* + \chi r_{RMS})}{N_A k_B T}\right] \tag{13}$$

where χ is a function describing how the pinning potential grows with the surface RMS roughness. The limited experimental studies investigating contact line motion on nanorough substrates[19,41−43] generally found that the roughness slows down the wetting process. Finally, recent modeling of droplet spreading dynamics[44,45] and molecular dynamic studies of imbibition into nanopores[46] also attempted to account for substrate nanotopography effects. However, the complexity of the proposed models and the number of assumptions upon which they are based makes it difficult to use them for experimental data interpretation.

In this investigation we study the dynamics of a TPCL on nanorough surfaces with diverse and well-characterized topography. The surface nanodefects vary in size, coverage, and shape, while the intrinsic surface chemistry and the two fluids (dodecane displacing water) remain the same as in our previous work.[1,2] Our focus is on the link between contact line dynamics and the nanoroughness parameters of the solid substrate.

EXPERIMENTAL PROCEDURES

Nanorough Substrates Preparation. Nanorough substrates with spherical asperities were prepared by depositing two different sizes of spherical silica nanoparticles (50 and 75 nm in diameter) on smooth microscope glass slides. Various surface coverages of the 75 nm

dx.doi.org/10.1021/ja3104846 | J. Am. Chem. Soc. 2013, 135, 7159−7171

nanoparticles (Klebosol, Clariant, France) were achieved by creating a particle density gradient on microscope glass slides. The slides were first cleaned by ultrasonication for 10 min in ethanol, then rinsed with ultrapure water (18.2 MΩ, TKA-GenPure, Huber & Co. AG Switzerland), and dried under a stream of high purity nitrogen (99.995%), before being washed in piranha solution (30 v % hydrogen peroxide and 70 v % fuming sulphuric acid) for 10 min and then thoroughly rinsed with ultrapure water. The samples were again dried under a pure nitrogen stream, exposed to air plasma for 2 min (RF level high, 0.1 Torr, PDC-32G, Harrick Plasma, USA), and without delay immersed for 2 h into a 2 v % solution of (3-aminopropyl)-triethoxysilane (APTES, ≥ 98%, Sigma-Aldrich, Germany) in toluene (for HPLC, Acros organics, Belgium) which was dried with molecular sieves. After adsorption, the samples were rinsed with ethanol and dried under a nitrogen stream. A 0.002 wt % dispersion of 75 nm diameter silica nanoparticles in purified water (house supply) was prepared and degassed just before use. The APTES-coated glass slides were mounted on a linear motion drive and immediately immersed to a depth of about 5 mm.[47] This initial immersion depth was predefined by a line on the sample and permitted subsequent orientation. The sample was then slowly immersed; the position of the sample was defined by an empirical function ($s(t) = at^2$; $a = 6.17 \times 10^{-6}$ mm·s^{-2}). During immersion, the suspension was gently agitated by a magnetic stirrer. The gradient length was set to 20 mm, and the immersion time was 30 min. After immersion, the sample was immediately removed, thoroughly rinsed with ultrapure water, and dried under a nitrogen stream. To anneal the APTES self-assembled monolayer (SAM), the freshly prepared samples were baked at 150 °C for 20 h.[48] Over the nanoparticle gradient, 8 distinct regions could be distinguished with surface defect coverages ranging from 0.8 to 19%, determined from AFM images, as described in the following section.

Deposition of the 50 nm diameter silica nanoparticles (Snowtec S20L Nissan Chemical) was performed following the experimental procedure described in detail in our previous work.[1] Functionalization of the bare glass slide with APTES followed the same steps as for the 75 nm gradient substrate, however the different surface coverages were achieved by dipping glass slides in nanoparticle dispersions whose concentrations varied between 0.1 and 0.4 mg/mL. Speeds of immersion and emersion were varied but kept constant for each individual run, using an automated dip-coater.[1] Eight nanorough surfaces with homogeneous particle coverage were produced, with defect coverages varying from 14 to 43%.

Surfaces covered with either pillars or cones were fabricated by using block copolymer micelle nanolithography for the formation of an etching mask and subsequent reactive ion etching (RIE) for pattern transfer.[49] Briefly, 50 mg of polystyrene-*block*-poly(2)-vinylpyridine, PS-*b*-P2VP (M_n(PS) = 110 000; M_n(PVP) = 52 000; M_w/M_n = 1.15; Polymersource) were dissolved in 10 mL of toluene leading to the formation of micelles, whose hydrophilic core can be loaded with a metal salt. Then $HAuCl_4 \cdot 3\ H_2O$ (Aldrich) was added to the micellar solution under stirring. The loading factor L ($L = n\{\text{metal salt}\}/n\{\text{P2VP}\}$) of the micelles was 0.5. Either glass or Suprasil were employed as substrates and immersed in piranha solution for at least 1 h, rinsed with ultrapure H_2O, and blown dry under a stream of nitrogen prior to the deposition of a micellar monolayer using an automated dip-coater (retraction speed: 12 mm/min). In order to remove the polymer matrix and reduce the Au^{III} to metallic Au, the samples were subsequently treated with hydrogen plasma (150 W, 0.4 mbar) for 45 min (Plasma System 100 from PVA TePla). The resulting highly ordered gold nanoparticle array acted as a mask upon subsequent reactive ion etching using an Oxford Plasmalab 80 RIE etcher. Glass substrates were etched in a mixture of Ar: SF_6: O_2 (10: 10: 5 sccm) as the process gas. The chamber pressure was set to 5 mTorr. Twenty-five W of RF power and 300 W ICP power were applied for 4 min at 20 °C. Suprasil samples were etched using a two-step RIE process. First, an Ar:SF_6 plasma was used (40:40 sccm, pressure: 50 mTorr). Etching was achieved by applying 120 W RF power for 45 s at 20 °C. Afterward the samples were etched in an Ar:CHF_3 plasma (40:40 sccm, pressure 50 mTorr) for 20 s using an RF power of 120 W and an ICP power of 20 W.

Finally, the chemistry of all the nanorough surfaces was controlled by depositing a fresh SAM of APTES on top of the various nanostructures, following protocols described previously.[1] The constancy of the substrate chemistry was probed by XPS and ToF-SIMS analysis, as documented in our previous work.[1] Thus the intrinsic surface chemistry of all substrates in this study is the same, and only the topography varies. A total of 18 different substrates, each featuring a specific set of 3 topographical parameters (defect shape, size, and spacing) were investigated.

Nanorough Substrate Characterization. The substrate surface topography was characterized by AFM and SEM measurements. AFM imaging of the surfaces was carried out under ambient conditions using an Asylum Research MFP-3D atomic force microscope in tapping mode. A minimum of 3 scan images (2×2 and/or 1×1 μm^2) were taken for each substrate and used to determine the actual defect height and coverage as well as the relevant Wenzel and RMS roughness factors. The RMS roughness, r_{RMS}, of the substrates was determined using the MFP3D software (Asylum Research, Igor pro, Wave Metrics). This same software was used to produce cross sections of the AFM images in order to measure the height, h, of the asperities. The images were analyzed using the WSXM software from Nanotech Electronica[50] enabling the substrates' Wenzel factor, r, defined as

$$r = \frac{A}{A_0} \tag{14}$$

to be calculated, where A is the actual surface area, denoted by the WSXM software as "ironed area", while A_0 is the projected area, i.e., the AFM scan area. The defect surface coverage in percentage, $C_{\%}$, and the number of defects (i.e., particles) per unit area, d, were determined using the image analysis software Image pro plus (Media Cybernetic).The area covered by each defect and their number were measured by setting a black and white threshold on the gray scale AFM images. In order to confirm the shape of the defects as well as the quality of their distribution at larger scales, images were taken on a Philips XL30 scanning electron microscope.

Wetting Experiments. Both static and dynamic wetting studies were performed using the same fluids as in our previous work,[2,51] namely Milli-Q water ($\rho = 10^3$ kg m^{-3}, $\eta = 8.9 \times 10^{-4}$ Pa s) and dodecane (99% Sigma Aldrich, $\rho = 7.5 \times 10^2$ kg.m^{-3}, $\eta = 1.34 \times 10^{-3}$ Pa s). The water−dodecane interfacial tension, γ, was 51.8 mN m^{-1} at 25 °C. Static and dynamic wettability studies were performed on all 18 nanorough surfaces as well as on reference, smooth APTES-coated surfaces. All measurements were conducted on a specially isolated, vibration free bench.

Static Wettability. Static advancing and receding contact angles of dodecane in water were measured using a captive bubble apparatus and OCA, SCA20, dataphysics software, as described previously.[2,51] Reproducible static contact angle data were obtained from a minimum of 5 measurements on each sample.

Dynamic Wetting Experiments and Data Processing. The top view experimental apparatus used to measure the dynamic contact angles has been described previously.[2,51,52] In brief, a specially designed microfluidic chip with a T-junction was designed as the base of a custom-made Teflon water container, on top of which the transparent nanorough substrates of interest were mounted face down. The microfluidic device released a microdroplet of dodecane (typically 300 μm in diameter) which rose freely in the water until it contacted the nanorough substrate surface. After thinning and rupture of the intervening water film, the dodecane drop displaced the surrounding water. The expansion of the contact area was monitored with an optical microscope (Olympus BXFM) connected to a high-speed video camera (Photron FastCam). For a minimum of 3 droplets spreading on each type of substrate, movies of 100−150 images were recorded at frame rates varying between 60 and 3000 fps. The volume of each droplet, V, was calculated from its diameter, measured from the first image recorded prior to film rupture at t_0. The time evolution of the contact area radius, R, was obtained from the subsequent images. The instantaneous dynamic contact angle with respect to the receding

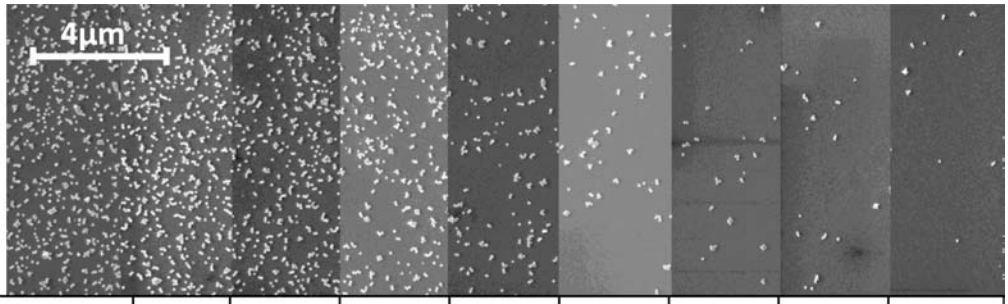

Coverage, %	19.1	15.6	9.7	8.2	6.2	3.9	2.4	0.9
Density, μm^{-2}	15.9	14.8	8.2	7.1	6.1	3.8	1.3	0.7

Figure 1. SEM images of the 75 nm nanoparticle gradient sample.

water phase was calculated using the spherical cap shape geometrical relationship:

$$R = \left(\frac{3V}{\pi}\right)^{1/3}\left[\frac{\sin^3\theta}{2 + 3\cos\theta - \cos^3\theta}\right]^{1/3} \quad (15)$$

The dimensionless bond number, $B = \Delta\rho g R_0^2/\gamma$, is used to make a quantitative assessment of capillary forces and gravity effects. Here $\Delta\rho$ is the density difference between the two fluids, g is the acceleration due to gravity, R_0 is the rest radius of the drop (i.e., before thin film rupture), and γ is the liquid−liquid interfacial tension. For the size range of the droplets studied (strictly <500 μm), $B < 1.1 \times 10^{-3}$. Thus, the influence of gravity on droplet's shape is not significant. No deformation of the drop was observed, and a good agreement between the calculated angle and the one determined optically from the side was confirmed experimentally.[19,52] The contact line velocity data were obtained using the software Origin 8. To minimize the scatter in the data at the slow end of droplet spreading, the radius data were fitted with a rational function of degree 3. The time derivative of the best fit gave the velocity of the three phase contact line, U.

RESULTS

Surface Topography. Representative AFM images and cross sections for different nanorough substrates as well as roughness analysis based on these AFM images are available in Figure A2 and Table A1, respectively). Using the 50 nm silica nanoparticles, substrates with surface coverages ranging from 14 to 53% were produced, while on the density gradient sample with 75 nm nanoparticles, the coverage varied between 1 and 20%. The difference in these coverages is due to the size-dependent diffusion mechanisms involved in the attachment of the nanoparticles onto the surface. It is discussed further in the Supporting Information. The nanolithography used to produce the pillar and cone nanostructures enables a much greater surface coverage to be achieved, namely 72 and 76%.

Typical SEM images of a 75 nm nanoparticle gradient are shown in Figure 1. Images of other substrates are given in the Supporting Information (Figure A3).

The silica particles formed spherical defects with overhangs, while the pillars appear to have straight walls and rather sharp angles at the top. The cones are well-defined. (Figure A3 in Appendix)

From the SEM images it appears that the coverage calculated from the AFM images probably includes a substantial error due to the final radius and opening angle of the AFM tip.[53] Indeed, for spheres with radius R, assuming submonolayer coverage with no nanoparticles touching or lying on top of others, the real coverage is given by $\Phi_r = d{\cdot}\pi R^2$, while the coverage measured by AFM with an AFM tip of radius r, is $\Phi_{AFM} = d{\cdot}\pi(R + r)^2$. Therefore AFM coverage data should be corrected by a factor $1/(1 + r/R)^2$. Since this correction was not applied to the coverage data reported here, these values are used as qualitative numbers only, for the sole purpose of ranking the various surfaces. Since the effect of overhangs in the calculation of the Wenzel and RMS roughness factors was not accounted for, the reported quantities should be regarded as minimum values. In the following quantitative analysis, the defect density values, d, which do not depend on the AFM tip radius, or defect shape are used.

For the spherical defect sizes, the Wenzel factor and the RMS roughness increase with particle density over the coverage range investigated. For an equivalent defect density, the RMS roughness is larger for a surface with larger defects (Figure 2).

Static Contact Angle and Hysteresis. The measured static contact angles are given in Figure A4. The behavior of the advancing and receding liquid−liquid interface is asymmetric for both 75 and 50 nm spherical defects. On one hand, the water receding contact angle decreases steadily as the defect spatial density increases.

In contrast, a rather large scatter was found for the advancing water contact angle, which does not seem to follow any clear trend for low defect densities but decreases sharply at the highest coverage. This behavior, in agreement with our previous results for 15 nm spherical defects,[1] is discussed in the following section.

In Figure 3 the static contact angle hysteresis is shown for all nanorough surfaces examined here and the surfaces decorated with 15 nm spherical defects, studied previously,[1] as a function of defect density.

The static contact angle hysteresis appears to pass through a maximum for each of the three different spherical defect sizes separately. The maximum in hysteresis is reached at a smaller defect density for the larger defects. We are aware that vibration may influence contact angle data and have explored this elsewhere.[54] Under the conditions used in these experiments, vibration effects are evidently of secondary importance.

Dynamic Wetting. *Dynamic Contact Angle.* In Figure 4 the dynamic water−dodecane receding contact angle is shown as a function of time for a smooth reference sample as well as two nanorough samples with 50 and 75 nm spherical defects at the same surface coverage (16%).

The dynamic contact angle behavior is generally the same on smooth and nanorough surfaces: It increases rather quickly at first and then slows down until it reaches a plateau. This plateau

dx.doi.org/10.1021/ja3104846 | J. Am. Chem. Soc. 2013, 135, 7159−7171

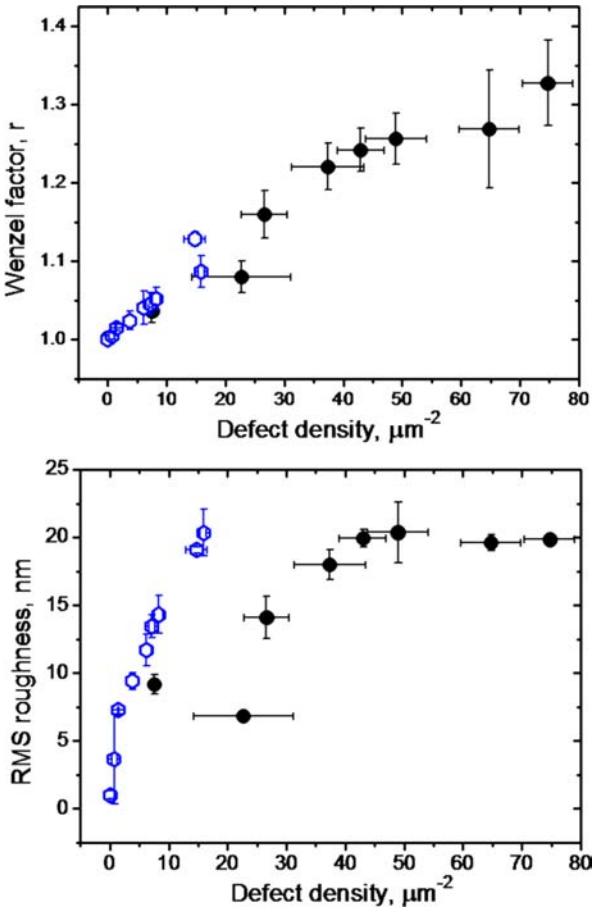

Figure 2. Wenzel factor and RMS roughness of the surfaces with spherical defects as a function of defect density; 50 nm (solid dots), 75 nm (open hexagons).

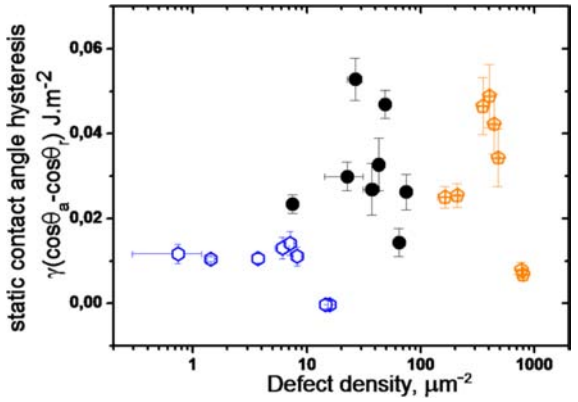

Figure 3. Static contact angle hysteresis as a function of spherical defect density; 15 nm (crossed pentagons), 50 nm (solid dots), 75 nm (open hexagons).

is reached much later on the nanorough surfaces: The contact angle still increases slowly when the measurements cease. In other words the static contact angle values are not reached within the time frame of the dynamic experiments, especially on the rougher surfaces where contact line motion is slower.

At equal surface coverage, contact line motion is slower on the surface with larger defects

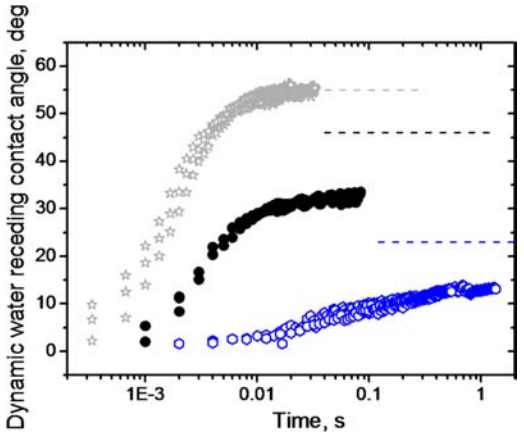

Figure 4. Dynamic receding contact angle of water as a function of time on smooth reference sample (star symbols), and nanorough surfaces with 50 (solid dots) and 75 nm (open hexagons) spherical defects at the same 16% coverage. The dashed lines show the respective static water receding contact angles.

Contact angle dynamics is independent of the droplet size in the size range studied, as shown in Figure A5 in Supporting Information.

Molecular Kinetic Theory. The molecular kinetic theory (eq 1) was fitted to the experimental data. In Figure 5, the cosine of

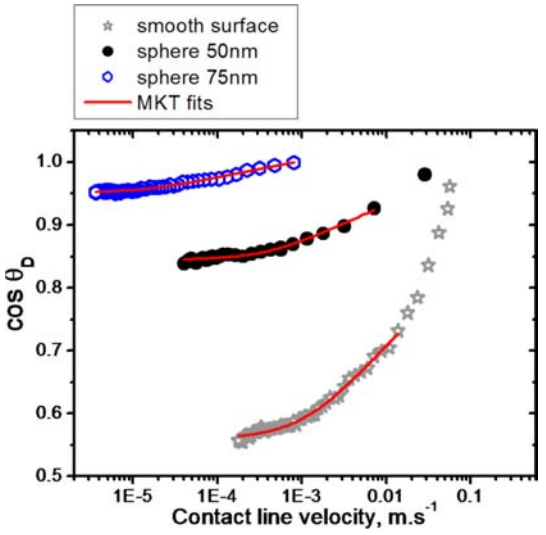

Figure 5. MKT fit for a typical set of experimental data (the same as the one shown in Figure 4), plotted as the cosine of the dynamic water contact angle as a function of the velocity of the TPCL.

the dynamic water contact angle is plotted as a function of the contact line velocity for the three surfaces shown in Figure 4 (a smooth reference surface and two nanorough samples with the same surface coverage (16%) of 50 and 75 nm spherical defects, respectively).

The MKT fits well the slow end of the motion, i.e., contact line velocities below 0.01 m/s. This indicates that close to the depinning threshold, the contact line motion is a thermally activated process. The wetting parameters, K_0 and λ, characterizing the thermally activated local displacements of the contact line were extracted from the MKT fits of the data sets for all surfaces and are shown in Figure 6 as a function of the relaxed

dx.doi.org/10.1021/ja3104846 | J. Am. Chem. Soc. 2013, 135, 7159−7171

receding water contact angle, that is θ_0^{MKT} (the third parameter extracted from the MKT fit) .

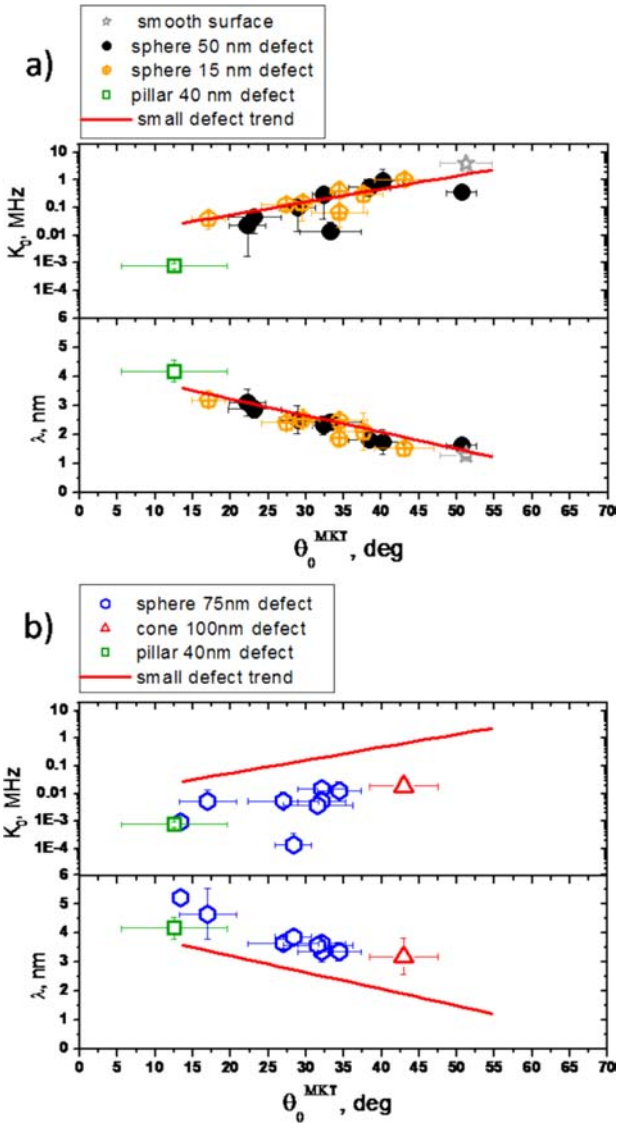

Figure 6. Contact line local displacement length, λ (nm), and frequency, K_0 (MHz), as a function of the relaxed receding water contact angle, θ_0^{MKT}, extracted from the MKT fit for nanodefects (a) ≤50 nm and (b) >50 nm. The solid red lines correspond to straight line fit.

For all nanorough surfaces, the displacement lengths are larger than expected for typical molecular adsorption−desorption processes. The λ values range from 1 to almost 6 nm. The displacement equilibrium frequencies decrease from almost 10 MHz on the smooth samples to <1 kHz on the roughest substrates.

For spherical defects up to 50 nm in size, the displacement length and frequency data all fall on a master curve when plotted against the relaxed receding water contact angle, θ_0^{MKT}.[3] The smooth surface data points also belong to these curves (Figure 6a). Larger defects (75 nm spheres and 100 nm cones) result in larger λ and smaller K_0 values, Figure 6b.

The 40 nm pillars, although they are within the size range up to 50 nm, result in substantially lower K_0 and larger λ values compared with the master curve.

Viscous relaxation time is given by $\tau = 6\pi\eta\xi^3/k_BT$, where ξ is the relevant length scale.[55] If we identify ξ with the displacement length λ, ranging from 5 down to 1 nm, then $1/\tau$ is in the range from 2 to 200 MHz. This is larger (faster relaxation) than the corresponding displacement frequencies K_0, thus the steady-state approach used in the following data interpretation is justified.

DISCUSSION

Static Wetting Properties. Surface nanoroughness has a significant impact on static contact angles both advancing and receding. The receding contact angle decreases with increasing roughness, as both defect coverage and defect size increase (Figure A4).

Static contact angle hysteresis is also affected by the surface nanoroughness. For a constant defect size, hysteresis increases at low surface coverage, passes through a maximum, and then decreases again. Similar behavior was previously observed for 15 nm spherical defects[1] and is clearly confirmed for the two larger size defects investigated here (Figure 3). Comparable behavior on nanorough surfaces has been reported by other groups.[34,36] We found that the change in slope for the hysteresis energy occurs for densities around 7.5, 50, and 400 defects per μm^2 for the 75, 50, and 15 nm diameter nanoparticles, respectively.

Low Defect Density Range. To evaluate whether or not the JG theory (eqs 8−12) is applicable to the present results, we first determined the energy dissipated on a single defect over a hysteresis cycle, W, from the experimental data. For the three spherical defect sizes, the hysteresis energy H obtained from the static advancing and receding contact angles (eq 7) was plotted as a function of the defect density, d. If the linear increase occurring at low defect densities corresponds to a hysteresis regime where single defects pin the contact line individually, then the JG model predicts[35]

$$H = \gamma(\cos\theta_r - \cos\theta_a) = H_0 + Wd \quad (16)$$

where H_0 is the hysteresis on the smooth sample, and W can be extracted by fitting the data with a straight line of a positive slope. Since the JG model is only applicable for low defect densities, the data points above the maximum of hysteresis were not included in the linear fits. The latter are shown in Figure 7a−c for the 75, 50, and 15 nm spherical defects, respectively, while the W values obtained from these fits are summarized in Table 1.

Although the scatter in the experimental data is significant, the values can be fitted with straight lines of positive slope up to the maximum hysteresis energy. These fits are rough approximations only, so that the W values are only qualitative guides. However, the values obtained are very similar to those found by Ramos et al.:[35] For defects in the 10 nm range, their W values range between 1 and 10×10^{-17} J. Furthermore, the present values suggest that the energy dissipated by one defect over a hysteresis cycle increases with the defect size, as anticipated.

W may now be evaluated from eq 11. The spring constant, k, is calculated from eq 10 using the water−dodecane interfacial tension and the static contact angle of water on a smooth surface $\theta_0 \approx (\theta^0_{adv} + \theta^0_{rec})/2 = 63°$, where $\theta^0_{adv} = 73°$ and $\theta^0_{rec} = 53°$ are the static advancing and receding contact angles of water on the smooth reference sample respectively.[56] Since the drop size is smaller than the capillary length (~4.5 mm), we set the cutoff length, L, equal to the drop diameter, which is

dx.doi.org/10.1021/ja3104846 | J. Am. Chem. Soc. 2013, 135, 7159−7171

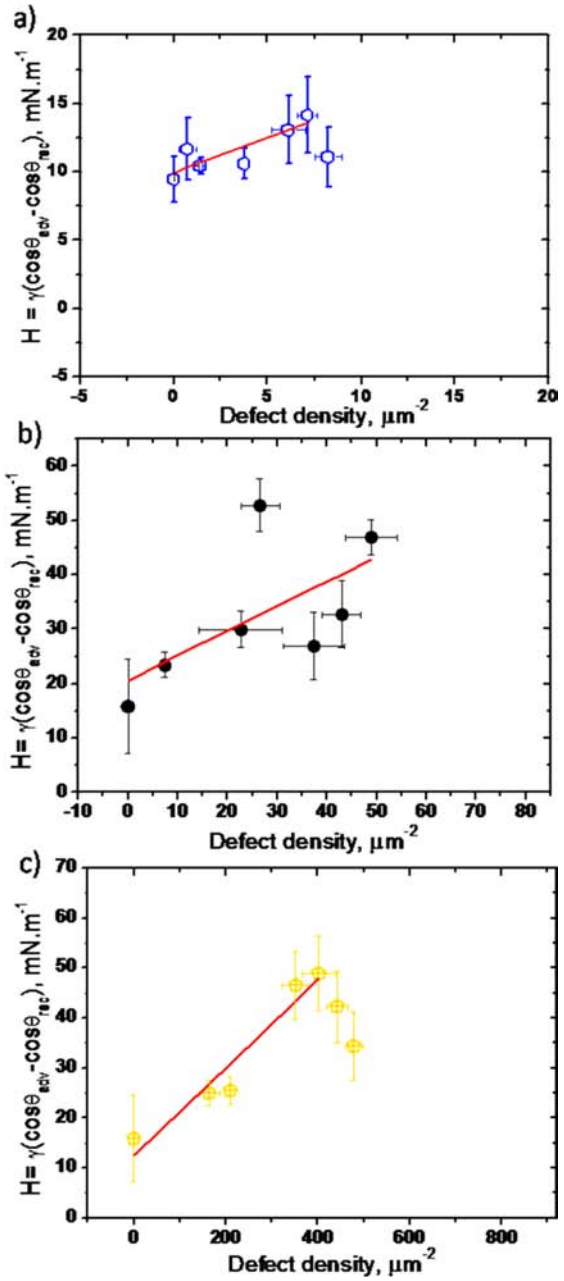

Figure 7. Hysteresis energy as a function of defect density for the nanorough surfaces with spherical defects; (a) 75 nm (open hexagons), (b) 50 nm (full dots), and (c) 15 nm (crossed pentagons). The solid red line correspond to the linear fits: (a) $H = 0.010(\mathrm{N{\cdot}m^{-1}}) + 5.14 \times 10^{-16}(\mathrm{N{\cdot}m}){\cdot}d$; (b) $H = 0.0206(\mathrm{N{\cdot}m^{-1}}) + 4.53 \times 10^{-16}(\mathrm{N{\cdot}m}){\cdot}d$; and (c) $H = 0.0125(\mathrm{N{\cdot}m^{-1}}) + 8.8 \times 10^{-17}(\mathrm{N{\cdot}m}){\cdot}d$. Linear fit region only are shown.

around 1 mm for the static wetting experiment. The values found for k are shown in Table 1. The evaluation of the defect force F_0 from eq 9 requires considerable care. The local slope, ϕ, in the equation should depend on the defect shape only and not on its size or spatial density. Thus it is reasonable to assume the same ϕ value when comparing substrates with spherical defects.

For spheres, considering that over a distance from the center of the defect to its edge ($\Delta x = r$), the defect height decreases from 2× radius to radius, $\Delta y = 2r - r = r$, then the mean slope $\Delta y/\Delta x = 1$, and an approximation of the local slope for the spherical defects is arctan(1) = 45° (see schematic in Figure A6a). Since the advancing and receding motion of the contact line is not symmetric (as shown by the advancing and receding contact angle data in Figure A4), we evaluate the pinning force independently for both directions of motion. For the advancing water phase:

$$|F_{0,\mathrm{adv}}| = h\gamma[\cos(\theta^0_{\mathrm{adv}} - \phi) - \cos\theta^0_{\mathrm{adv}}] \tag{17}$$

Similarly, for a receding water front:

$$|F_{0,\mathrm{rec}}| = h\gamma[\cos(\theta^0_{\mathrm{rec}} + \phi) - \cos\theta^0_{\mathrm{rec}}] \tag{18}$$

From eqs 8 and 11, for asymmetric advancing and receding defect forces, the energy dissipated on a single defect over a hysteresis cycle is

$$W = W_d^{\mathrm{adv}} + W_d^{\mathrm{rec}} = \frac{F_{0,\mathrm{adv}^2}}{2k} + \frac{F_{0,\mathrm{rec}^2}}{2k} \tag{19}$$

The $W(h,\theta_0,\phi)$ numerical values calculated using eqs 19 for all spherical defects are reported in Table 1. These values will be referred to as W_{calc} to distinguish them from the W_{plot} data extracted from Figure 7.

For spherical defects from 15 to 75 nm, the W_{calc} values (eq 19) increase with defect size and are of the same order of magnitude as the values extracted from Figure 7. This is quite reassuring as the equations used to calculate the pinning energy on a single defect do not account for the exact shape of the defect (locally varying slope, overhangs, etc). However, W_{calc} is consistently smaller than W_{plot}, a feature which may have several causes. First, the 45° defect slope chosen to estimate W_{calc} may be underestimated. From SEM images (Figure A6b), the spherical defects have an overhang, and thus, the effective defect slope may be much higher than 45°.

However, calculation of the defect forces $F_{0,\mathrm{adv}}$ and $F_{0,\mathrm{rec}}$ using eqs 17 and 18 is only valid for $\theta_0 - \phi > 0$ and $\theta_0 + \phi < 180°$, respectively (see appendix Figure A6c and related discussion). An estimate of the effect of the defect slope on W_{calc} is shown in Table 1, where the parameters obtained for the 75 nm spherical particles are shown for the case where the maximum slope for which both eqs 17 and 18 are still valid is chosen ($\phi = 70°$). An increase in the defect slope leads to an

Table 1. Theoretical Roughness Parameters Used in the JG Model (Defect Size h and Slope ϕ) for the Spherical Defects[a]

defect shape	defect size, nm	local slope	k (eq 8) mN/m	$F_{0,\mathrm{adv}}$ 10^{-9} N	$F_{0,\mathrm{rec}}$ 10^{-9} N	W_{calc} 10^{-17} J	W_{plot} 10^{-17} J
sphere	15 ± 5	45	11.6	0.46	0.58	2.3	8.8
sphere	50 ± 5	45	13.0	1.5	1.9	23	45.3
sphere	75 ± 5	45	13.6	2.3	2.9	50	51.4
sphere	75 ± 5	70	13.6	2.7	4.5	101	51.4

[a]Corresponding calculated spring constant, k; single defect advancing and receding pinning force, F_0; pinning energy W_{calc} from eq 19; and pinning energy extracted from Figure 7, W_{plot}.

dx.doi.org/10.1021/ja3104846 | J. Am. Chem. Soc. 2013, 135, 7159−7171

increase in W_{calc}. A second reason for the deviation between W_{calc} and W_{plot} could be that the eqs 10 and 17−19 oversimplify the situation. For example local defect slopes are too large; overhangs are present with possible trapping of one fluid phase in the wedges. Defects may already be correlated even at small defect densities, thus the energy dissipated over a hysteresis cycle may be larger than if the contact line was just pinned on single defects. Furthermore, some nanoparticles may rest on others, thus forming defects with considerably larger size and higher pinning strength.

High Defect Density. The JG model cannot describe static contact angle hysteresis at high defect densities. Several groups have attempted to tackle this intricate case.[35,39,57] Generally, a critical defect density, d_c, above which the hysteresis does not vary linearly with defect density is found. For defects in the micrometer range Di Meglio et al.[39] found $d_c \approx 1/L_c^2$, while Crassous and Charlaix[57] reported $d_c \approx 30/h^2$ above which the collective effect of the surface asperities results in a decrease in hysteresis. For the present systems these expressions correspond to a critical density, d_c, of ∼1000 μm^{-2}, which means that all of the data should fall in the low defect density regime. This is clearly not the case and suggests that the outcomes for micrometer size defects do not apply to the present case of nanometer dimension defects and rather small spreading droplets. Joanny and de Gennes originally considered that the dilute defect regime was valid for $dh^2 \ll 1$. In the present system, a transition in the hysteresis energy slope was found for dh^2 in the range between 0.04 and 0.13, but even the largest values of dh^2 (i.e., above the transition) do not exceed 0.2. Thus the threshold given by Joanny and de Gennes confirms the regime of pinning on single defects below the transition but does not allow any further conclusion about the regime above the change in the hysteresis energy slope. In their study of the pinning of the contact line on nanorough surfaces, Ramos et al.[35] explain the decrease in hysteresis at high defect density not only by collective pinning on dense defects but also with the possible formation of air cavities along the wetting front. From an energy analysis of the elastic and pinning energies, they derived a critical defect density above which such phenomena should occur in liquid−gas systems. In their approach the critical defect density is proportional to $1/h^2$, in good agreement with the present results, with a maximum in hysteresis reached at smaller coverages for larger defects. Furthermore, they estimated the maximum screening length, L_c, over which the elastic contact line would deform before the formation of nanobubbles occurs, as

$$L_c \approx \frac{\gamma \sin^2 \theta_0}{dF_0} \tag{20}$$

The maximum screening length for the present system, is calculated following the Ramos et al.[35]approach. Using eq 9 and inserting the average distance between defect, $l_a = 1/hd$, in eq 20, one obtains $L_c \approx (l_a \sin^2 \theta_0)/(\cos(\theta_0 - \phi) - \cos \theta_0)$. L_c is proportional to the average distance between defects, $1/hd$, through a factor $(\sin^2\theta_0)/(\cos(\theta_0 - \phi) - \cos \theta_0) > 1$. Since the distance between defects is systematically shorter than the correlation length, the condition for the formation of trapped air bubbles is verified for all nanorough surfaces in the present study. The phenomenon of air trapping is well-known to occur for water in air on very rough hydrophobic surfaces (micrometer range) and for superhydrophobic surfaces with combined micro and nanoroughness. A similar effect may well occur for dodecane in water, the system studied here, with trapping of water nanodroplets under the dodecane drop as it spreads. In Figure A7, we show that small air bubbles or water droplets trapped under the dodecane drop could be directly observed optically in the top view images for the roughest substrates. One expects equivalent phenomena for the surfaces with smaller roughness, with smaller quantities of one fluid or the other trapped under single defect overhangs or between defects. In this case, the droplets of trapped fluid could be as small as several hundreds of nanometers, thus not visible optically. Furthermore, analysis of the TPCL friction coefficient revealed that as the defect density increases, the friction appears to pass through a maximum, before decreasing again. This result, described in the Supporting Information (Figure A8), is consistent with the formation of trapped water droplets at high defect densities: The presence of trapped fluid in between defects at high defect densities screens the roughness and thus the frictional resistance to contact line motion.

Dynamic Wetting. The unbalanced Young force is the driving force for the TPCL motion. The fact that the contact line velocity as a function of driving force relationship follows the molecular kinetic theory shows that the displacement process occurring at the contact line is thermally activated. Thermal fluctuation attempts to depin or unstick the contact line and success or failure depend on the energy barriers between two pinning "sites". These energy barriers of course may depend on the strength of the chemical interaction between the solid and the fluid (i.e., static contact angle) and/or on the surface nanodefect pinning strength.[58] Residual background vibration may contribute to the thermally activated effects, yet since the vibrational noise must be comparable in all experiments, any trend observed in the dynamic contact angle behavior as the nanoroughess increases must be dominated by the increasing roughness rather than by the background vibrations.

The local displacement length, λ, increases with surface roughness (Figure 6) but does not match the size of the defect. At the microscopic scale in the three phase zone, pinning on a single defect may not be the sole mechanism, and defect correlation may well decrease the value found for λ. Using the linearized form of the MKT approach, as adopted by Prevost et al.[16] still yields λ values close to those of the full MKT approach.

The molecular kinetic parameters obtained for pillars and cones differ from the ones obtained for spherical defects of a similar defect size (Figure 6). The λ values are larger, and K_0 are significantly smaller, suggesting a slower motion process with larger elemental displacements. Such behavior could be attributed to the effect of sharp edges increasing the pinning potential of these defects and thus hindering the contact line motion more strongly than on spherical defects.

Wetting Activation Free Energy. The MKT was used to extract the activation free energy of wetting, ΔG_w^*, from eq 2. In Figure 8, the effects of (a) apparent surface wettability and (b) defect coverage on the specific activation free energy of wetting, $\Delta g_w^* = \Delta G_w^*/\lambda^2 N_A$, are shown. Δg_w^* decreases steadily with decreasing static water contact angle, with globally lower Δg_w^* for the large defects, i.e., 75 nm sphere and 70 nm cones (Figure 8a). The change in static contact angle reflects changes in surface topography rather than surface chemistry, since the latter is the same for all substrates. If the activation energy was solely determined by the surface chemistry, it should be the same for all substrates. Since Δg_w^* is clearly not

dx.doi.org/10.1021/ja3104846 | J. Am. Chem. Soc. 2013, 135, 7159−7171

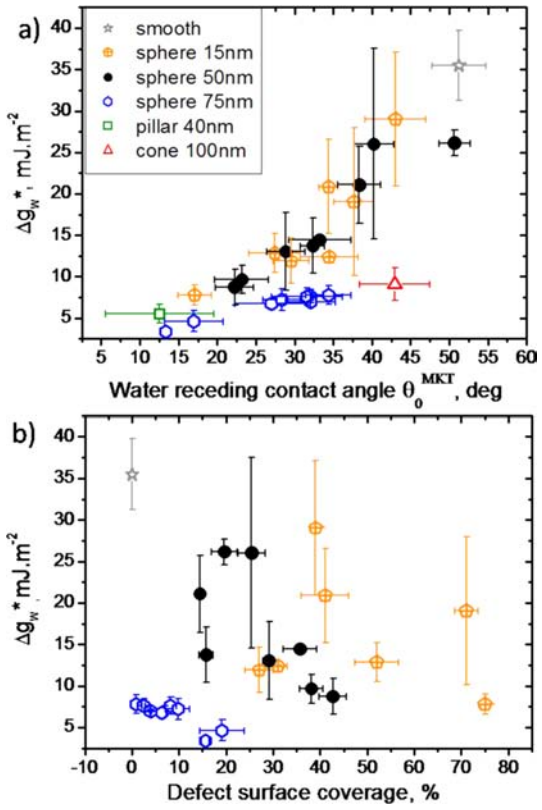

Figure 8. Normalized activation free energy of wetting as a function of (a) the water receding static contact angle extracted from the MKT fits and (b) defect surface coverages.

independent of the presence, size, density, and shape of the nanodefects, it is certainly not governed by surface chemistry alone.

Δg_w* appears to pass through a maximum as the defect density increases, with this maximum occurring at a smaller coverage for the larger defects (Figure 8b). This is similar to the hysteresis behavior (Figure 3). The smallest ΔG_w* value (not normalized to λ^2) is found for the smooth surface and increases with roughness.

The influence of the apparent wettability (work of adhesion) cannot be neglected, and it is likely that the activation free energy of wetting results from the combination of surface wettability and topography.

The relative importance of solid–fluid interactions and pinning–depinning processes to the energy barrier associated with the thermally activated mechanism controlling contact line motion is now assessed. When considering that contact line motion is governed by the chemical interaction between the solid and the fluid, Blake and De Coninck[8] suggested that the surface component of Δg_w* could be equated to the work of adhesion of the liquid (eq 5). In this approach, developed for liquid–vapor systems, W_a is the inherent work of adhesion obtained using the Young contact angle θ_0. This inherent work of adhesion is determined by surface chemistry alone and is not affected by the presence of topographical defects, thus it is the same for all surfaces investigated here.

In our work on liquid–liquid displacement on nanorough surfaces, where the activation free energy of wetting varies with surface topography, a better correlation was obtained with the apparent work of adhesion of the advancing liquid phase, where the latter is substantially affected by roughness:

$$W_a^* = \gamma(1 + \cos \theta_{\text{adv dodecane}}^*) \quad (21)$$

where γ is the water–dodecane interfacial tension and $\theta_{\text{adv dodecane}}$* is the apparent static advancing contact angle of dodecane. W_a* and Δg_w* are compared in Figure 9a. Although the two quantities are of the same order of magnitude, W_a* is consistently smaller than Δg_w*, except for the cones as well as 50 and 75 nm spheres at high densities. The apparent work of adhesion generally underestimates the energy required to induce contact line motion.

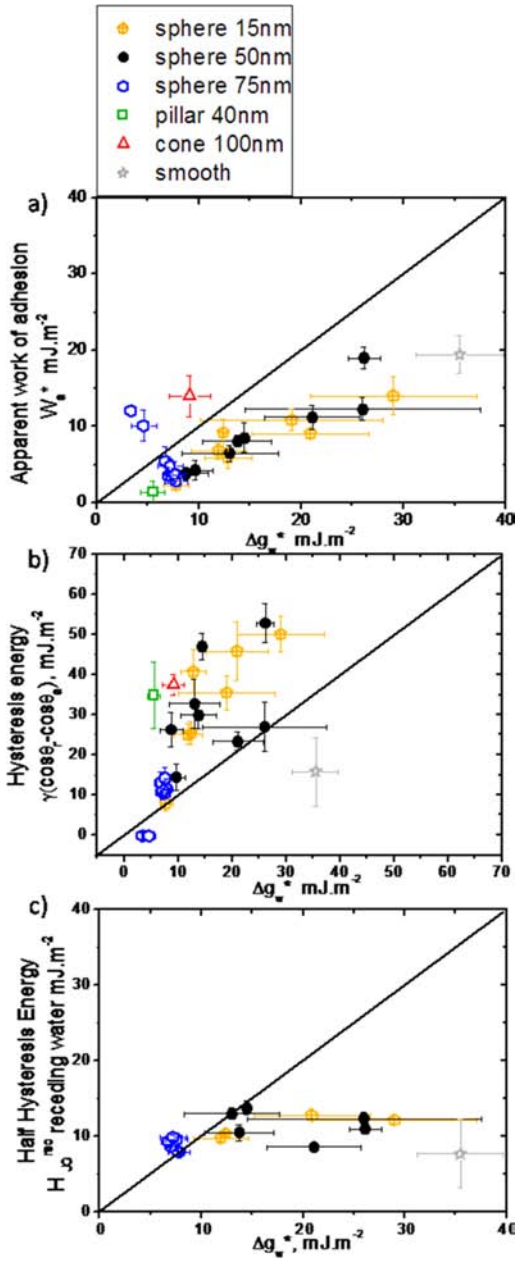

Figure 9. The specific activation free energy, Δg_w* compared with (a) the apparent work of adhesion, W_a*, of dodecane in the presence of water. (b) The hysteresis energy, H, calculated from the static advancing and receding contact angles value (eq 7), and (c) the half hysteresis calculated from the JG model for the water receding contact line. Only the data points corresponding to low surface coverage (below maximum of hysteresis) are presented. The 1/1 lines is simply a guide for the eyes.

dx.doi.org/10.1021/ja3104846 | J. Am. Chem. Soc. 2013, 135, 7159–7171

To assess whether or not the energy barriers hindering the contact line motion correlate with the pinning strength of the surface, the specific activation free energy of wetting Δg_w^* is also compared with the hysteresis energy, H, calculated from the static advancing and receding contact angle values (eq 7) in Figure 9b. The two quantities are of the same order of magnitude, however, H is consistently larger than Δg_w^* and overestimates the characteristic activation energy for contact line motion.

From the results shown in Figure 9a,b, one cannot decide whether the work of adhesion or hysteresis energy better correlates with the free activation energy of wetting.

Our results are in accord with the prescient observation of Rolley and Guthmann,[17] who proposed that contact line pinning on nanodefects could control both static contact angle hysteresis as well as contact line dynamics. However, we question the legitimacy of this comparison between hysteresis energy and the activation free energy of wetting as determined in our system. The hysteresis energy is evaluated from the experimental data for advancing and receding static contact angles and thus accounts for both advancing and receding directions of contact line motion. In contrast to the work by Rolley and Guthmann, in our study the activation free energy of wetting is extracted from the MKT fit to the experimental data for the dynamic displacement of water by dodecane, i.e., only one direction of motion is considered.

In order to compare the specific activation free energy of wetting with the hysteresis energy corresponding to one direction of contact line motion only, we adopt the JG approach. We define the half hysteresis, H_{JG}^{rec} in the direction of dodecane displacing water as

$$H_{JG}^{rec} = H_0^{rec} + dW_d^{rec} \tag{22}$$

where $H_0^{rec} = \gamma(\cos\theta_{rec}^0 - \cos\theta_0)$, θ_{rec}^0 is the static receding contact angle of water on the smooth reference sample and $W_d^{rec} = F_{0,rec}{}^2/2k$ is calculated from eqs 10 and 18. The correlation between H_{JG}^{rec} and the specific activation free energy of wetting is shown in Figure 9c.

As mentioned before, this approach is only valid for dilute defects, thus the data corresponding to the substrate with high defect densities are not presented. The theoretical receding part of the hysteresis energy, calculated from the pinning strength of single defects is smaller than the activation free energy.

If both the surface chemistry and pinning on a topographical defect were to equally contribute to the energy barrier regulating the three phase contact line motion, then a simple sum of the two components (pinning energy for the dodecane advancing against water and apparent work of adhesion of dodecane in water) should return the wetting activation free energy value:

$$\Delta g_w^* = W_a^* + H_0^{rec} + dW_d^{rec} \tag{23}$$

The validity of eq 23 is examined in Figure 10. The experimental data are in good agreement with eq 23, within experimental error. Within the limit of low defect densities, eq 23 successfully expresses the specific activation free energy of wetting as a function of both surface chemistry and topography for nanodefects. Using the JG model, this approach directly accounts for the substrate topography. The defect density d, the defect height h, and the defect slope ϕ (through the pinning force F_0 in eq 18) are all explicitly accounted for in eq 23.

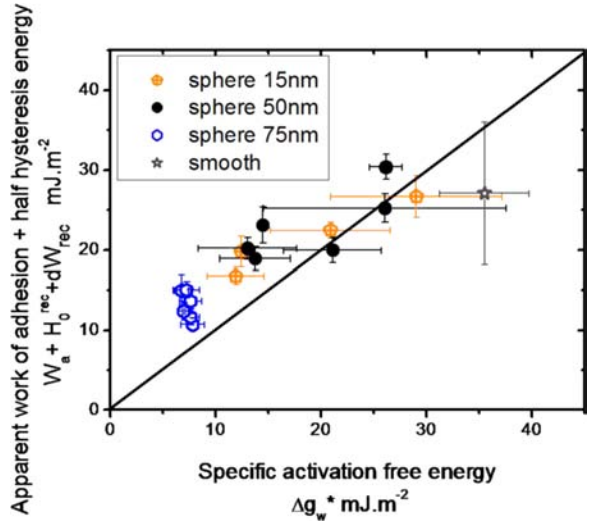

Figure 10. For defect densities below the maximum hysteresis, the sum of the apparent work of adhesion of dodecane in water and the half hysteresis for the direction of flow when dodecane displaces water (eq 23) is plotted as a function of the specific activation free energy of wetting.

It is also worth noting that although viscous dissipation does not appear as a separate term in eq 23, the influence of viscous dissipation on the overall contact line motion enters the molecular kinetic model via the viscous contribution to the activation free energy of wetting (eq 4). Thus, it is already included in the MKT fitting of the data, where ΔG_v^* was allowed to be nonzero. Yet accounting for the direct contribution of viscous dissipation could provide a more comprehensive description of the phenomenon and would be a very interesting object for future work.

CONCLUSIONS

Using nanoparticle assembly and nanofabrication methods, the nanotopography of solid surfaces has been varied in a controlled fashion, and its effect on both static wettability and contact line dynamics in a solid−liquid−liquid system examined. By focusing on the specific influence of the surface nanoroughness for a fixed surface chemistry, we demonstrate that both static and dynamic wetting are sensitive to changes in surface topography at the nanoscale.

The static contact angle hysteresis passes through a maximum as the nanodefect density increases, with the maximum observed at a lower critical defect density for larger defects. The linear increase in hysteresis observed in the low defect density range has been interpreted in terms of the JG theory[28] for pinning on single defects. The JG model provides a reasonable description of the hysteresis energy for the systems examined. Our observations are in agreement with those of Delmas et al.[36] who found that the JG model, originally derived for microscopic heterogeneities, applies to physical defects in the nanometer size range. The first evidence for the validity of Joanny and de Gennes' theory in describing hysteresis in a solid−liquid−liquid system is provided in the present study.

At high defect densities, the decrease in hysteresis and contact line friction coefficient indicates that a more complicated wetting state, involving the trapping of water droplets underneath the dodecane drop, occurs.

Roughness systematically slows down contact line motion. The molecular kinetic theory qualitatively describes the

dx.doi.org/10.1021/ja3104846 | J. Am. Chem. Soc. 2013, 135, 7159−7171

displacement of water by dodecane at low velocities, confirming that the contact line events are thermally activated on all types of surface examined. The molecular kinetic parameters extracted from the MKT fits are consistent with a composite mechanism involving concomitant adsorption−desorption processes and pinning−depinning events. This hypothesis was tested in several ways. The specific activation free energy of wetting, Δg_w^*, was influenced by both solid−liquid surface interactions and surface pinning strength, as summarized schematically in Figure 11. In the presence of sharp edges, Δg_w^* is even more sensitive to the surface roughness.

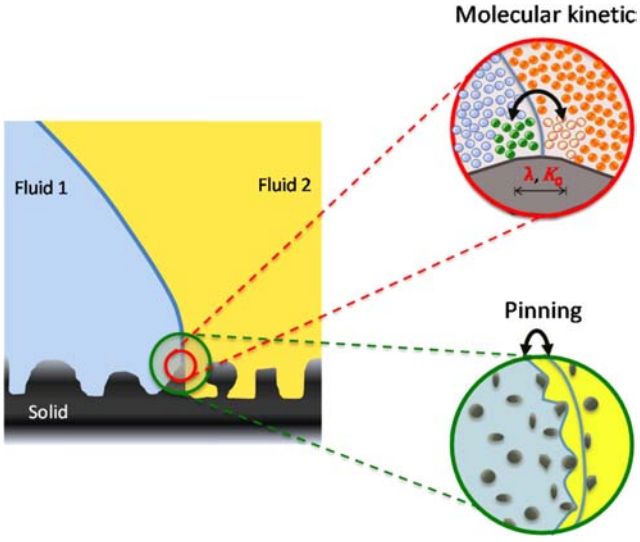

Figure 11. Scheme of the two parallel mechanisms contributing to the energy barriers hindering contact line motion.

For the one direction of motion investigated (dodecane displacing water), comparison of Δg_w^* with the apparent work of adhesion of dodecane showed that the latter underestimates the energy necessary to induce contact line motion. Similarly, the hysteresis energy calculated from the JG theory for receding water is not sufficient to be solely responsible for the energy barrier hindering contact line motion. Taken together, however, the sum of these two energy terms (eq 23) corresponds rather well to Δg_w^*. Thus at a nanoscopic level, the wetting activation free energy is directly connected to surface nanotopography, and its complex relation to roughness seems to be captured by eq 23.

We hope that our original results yield useful insights and pave the way for future work on the role of surface nano and microroughness in dynamic wetting. Our understanding of many natural phenomena and industrial processes where liquids displace other liquids over surfaces will benefit greatly from such developments.

■ ASSOCIATED CONTENT

Supporting Information

Nanorough surfaces topography analysis, static advancing and receding contact angles data, spherical defect slope discussion, illustration of fluid trapping on the roughest substrate, and contact line friction discussion are disclosed in appendix. This material is available free of charge via the Internet at http://pubs.acs.org.

■ AUTHOR INFORMATION

Corresponding Author

john.ralston@unisa.edu.au

Present Addresses

[†]Karlsruhe Institute of Technology, 76021 Karlsruhe, Germany.
[‡]In exchange at the IWRI from the Laboratory for Surface Science and Technology, Department of Materials, ETH Zurich.
[§]Department of New Materials and Biosystems, Max Planck Institute for Intelligent Systems, Heisenbergstraße 3, D-70569 Stuttgart, Germany

Notes

The authors declare no competing financial interest.

■ ACKNOWLEDGMENTS

We are very grateful to the Australian Research Council for the financial support that made this work possible through the Discovery Project scheme. In addition financial support by the BMBF (Federal Ministry of Education and Research, project EFFET, contract no. 13N9713, and project PhoNa, contract no. 03IS2101E) and the Max Planck Society is acknowledged.

■ REFERENCES

(1) Ramiasa, M.; Ralston, J.; Fetzer, R.; Sedev, R. *J. Phys. Chem. C* **2012**, *116*, 10934.
(2) Ramiasa, M.; Ralston, J.; Fetzer, R.; Sedev, R. *J. Phys. Chem. C* **2011**, *115*, 24975.
(3) Blake, T. D.; Haynes, J. M. *J. Colloid Interface Sci.* **1969**, *30*, 421.
(4) Blake, T. D. *J. Colloid Interface Sci.* **2006**, *299*, 1.
(5) Bonn, D.; Eggers, J.; Indekeu, J.; Meunier, J.; Rolley, E. *Rev. Mod. Phys.* **2009**, *81*, 739.
(6) Blake, T. D.; De Coninck, J. *Adv. Colloid Interface Sci.* **2002**, *96*, 21.
(7) Blake, T. D. In *Wettability*; Berg, J., Ed.; Marcel Dekker Inc: New York, 1993, p 251.
(8) Blake, T. D.; Shikhmurzaev, Y. D. *J. Colloid Interface Sci.* **2002**, *253*, 196.
(9) Phan, C. M.; Nguyen, A. V.; Evans, G. M. *Langmuir* **2003**, *19*, 6796.
(10) Wang, X.; Nguyen, A. V.; Miller, J. D. *Int. J. Miner. Process.* **2006**, *78*, 122.
(11) Voué, M.; Rioboo, R.; Adao, M. H.; Conti, J.; Bondar, A. I.; Ivanov, D. A.; Blake, T. D.; De Coninck, J. *Langmuir* **2007**, *23*, 4695.
(12) Vega, M. J.; Gouttière, C.; Seveno, D.; Blake, T. D.; Voué, M.; Coninck, J. D. *Langmuir* **2007**, *23*, 10628.
(13) Li, H.; Sedev, R.; Ralston, J. *Phys. Chem. Chem. Phys.* **2011**, *13*, 3952.
(14) Petrov, J. G.; Ralston, J.; Schneemilch, M.; Hayes, R. A. *J. Phys. Chem. B* **2003**, *107*, 1634.
(15) Petrov, J. G.; Ralston, J.; Schneemilch, M.; Hayes, R. A. *Langmuir* **2003**, *19*, 2795.
(16) Prevost, A.; Rolley, E.; Guthmann, C. *Phys. Rev. Lett.* **1999**, *83*, 348.
(17) Rolley, E.; Guthmann, C. *Phys. Rev. Lett.* **2007**, *98*, 166105.1.
(18) Rolley, E.; Guthmann, C.; Pettersen, M. S. *Phys. Rev. Lett.* **2009**, *103*, 016101.1.
(19) Fetzer, R.; Ralston, J. *J. Phys. Chem. C* **2010**, *114*, 12675.
(20) Johnson, R. E.; Dettre, R. H. In *Contact Angle, Wettability, and Adhesion*; American Chemical Society: Washington, D.C., 1964; Vol. *43*, p 112.
(21) Neumann, A. W. *Adv. Colloid Interface Sci.* **1974**, *4*, 105.
(22) Eick, J. D.; Good, R. J.; Neumann, A. W. *J. Colloid Interface Sci.* **1975**, *53*, 235.
(23) Huh, C.; Mason, S. G. *J. Colloid Interface Sci.* **1977**, *60*, 11.
(24) Busscher, H. J.; van Pelt, A. W. J.; de Boer, P.; de Jong, H. P.; Arends, J. *Colloids Surf.* **1984**, *9*, 319.

(25) Shanahan, M. E. R. *Langmuir* **1995**, *11*, 1041.
(26) Shanahan, M. E. R.; Sefiane, K. *Kinetics of Triple Line Motion during Evaporation*; Brill Publishers: Leiden, The Netherlands, 2009.
(27) Bormashenko, E.; Musin, A.; Zinigrad, M. *Colloid Surf., A* **2011**, *385*, 235.
(28) Joanny, J. F.; De Gennes, P. G. *J. Chem. Phys.* **1984**, *81*, 552.
(29) Dietrich, S.; Popescu, M. N.; Rauscher, M. *J. Phys.: Condens. Matter* **2005**, *17*, S577.
(30) Drelich, J.; Miller, J. D. *Langmuir* **1993**, *9*, 619.
(31) Drelich, J. *Pol. J. Chem.* **1997**, *71*, 525.
(32) Checco, A.; Guenoun, P.; Daillant, J. *Phys. Rev. Lett.* **2003**, *91*, 186101.1.
(33) Checco, A.; Schollmeyer, H.; Daillant, J.; Guenoun, P.; Boukherroub, R. *Langmuir* **2005**, *22*, 116.
(34) Ramos, S. M. M.; Charlaix, E.; Benyagoub, A.; Toulemonde, M. *Phys. Rev. E* **2003**, *67*, 031604.1.
(35) Ramos, S.; Tanguy, A. *Eur. Phys. J. E: Soft Matter Biol. Phys.* **2006**, *19*, 433.
(36) Delmas, M.; Monthioux, M.; Ondarcuhu, T. *Phys. Rev. Lett.* **2011**, *106*, 136102.1.
(37) Cox, R. G. *J. Fluid Mech.* **1983**, *131*, 1.
(38) Nadkarni, G. D.; Garoff, S. *Europhys. Lett.* **1992**, *20*, 523.
(39) Di Meglio, J. M. *Europhys. Lett.* **1992**, *17*, 607.
(40) Semal, S.; Blake, T. D.; Geskin, V.; de Ruijter, M. J.; Castelein, G.; De Coninck, J. *Langmuir* **1999**, *15*, 8765.
(41) Modaressi, H.; Garnier, G. *Langmuir* **2002**, *18*, 642.
(42) Xue, L.; Hu, B.; Han, Y. *J. Chem. Phys.* **2008**, *129*, 214902.1.
(43) Girardo, S.; Palpacelli, S.; De Maio, A.; Cingolani, R.; Succi, S.; Pisignano, D. *Langmuir* **2012**, *28*, 2596.
(44) Savva, N.; Kalliadasis, S. *Phys. Fluids* **2009**, *21*, 092102.
(45) Nikos, S.; Serafim, K. *J. Phys.: Conf. Ser.* **2010**, *216*, 012017.1.
(46) Stukan, M. R.; Ligneul, P.; Crawshaw, J. P.; Boek, E. S. *Langmuir* **2010**, *26*, 13342.
(47) Huwiler, C.; Kunzler, T. P.; Textor, M.; Vörös, J.; Spencer, N. D. *Langmuir* **2007**, *23*, 5929.
(48) Wang, W.; Vaughn, M. W. *Scanning* **2008**, *30*, 65.
(49) Morhard, C.; Pacholski, C.; Lehr, D.; Brunner, R.; Helgert, M.; Sundermann, M.; Spatz, J. P. *Nanotechnology* **2010**, *21*, 425301.1.
(50) Horcas, I. *Rev. Sci. Instrum.* **2007**, *78*, 013705.1.
(51) Fetzer, R.; Ramiasa, M.; Ralston, J. *Langmuir* **2009**, *25*, 8069.
(52) Fetzer, R.; Ralston, J. *J. Phys. Chem. C* **2009**, *113*, 8888.
(53) Mulvaney, P.; Giersig, M. *J. Chem. Soc., Faraday Trans.* **1996**, *92*, 3137.
(54) Fabretto, M.; Sedev, R.; Ralston, J. In *Contact Angle, Wettability and Adhesion*; Mittal, K. L., Ed.; CRCBoca Raton, FL , 2003; Vol. *3*, p 161.
(55) Petit, J.; Rivière, D.; Kellay, H.; Delville, J.-P. *Proc. Natl. Acad. Sci., U.S.A.* **2012**, *109*, 18327.
(56) In *Fundamentals of Interface and Colloid Science*; Lyklema, J., Fleer, G. J., Kleijn, J. M., Leermakers, F. A. M., Norde, W., Vliet, T. v., Eds.; Academic Press: Waltham, MA, 2000; Vol. *3*, p 1.
(57) Crassous, J.; Charlaix, E. *Europhys. Lett.* **1994**, *28*, 415.
(58) Slavchov, R.; Dutschk, V.; Heinrich, G.; Radoev, B. *Colloids Surf., A* **2010**, *354*, 252.